



Proton Conduction and Electrochemical Performance of La/Pr co-Doped Ceria Electrolyte in Ceramic Fuel Cell

Xinlei Yang¹ · Fan Yang¹ · Muhammad Afzal² · Wanli Sun¹ · Jung-Sik Kim³

Received: 8 February 2023 / Revised: 16 June 2023 / Accepted: 21 June 2023 / Published online: 27 October 2023
© The Author(s), under exclusive licence to Korean Society for Precision Engineering 2023

Abstract

La/Pr co-doped ceria (LCP) is processed to fabricate low-temperature ceramic fuel cell based on industrial-grade rare-earth carbonate electrolyte that is reached above a maximum power density of 750 mW/cm² at 520 °C. The charge carriers are investigated through LCP fuel cell having symmetric NCAL (Ni_{0.8}Co_{0.15}Al_{0.05}LiO_{2-δ}) electrodes using proton conductor BCZY (BaCe_{0.7}Zr_{0.1}Y_{0.2}O_{3-δ}) as a blocking layer and are found protons that dominate during the cell operation. The results of associated characterizations for HCC (hydrogen concentration cell) and the OCC (oxygen concentration cell) reveal that LCP material is mixed conductor of both protons and oxygen ions simultaneously. Transmission electron microscopy (TEM), X-ray Photoelectron Spectroscopy (XPS) and Fourier-transform infrared spectroscopy (FTIR) analysis before and after the electrochemical testing of the cell are performed which show an amorphous layer of LiOH/Li₂CO₃ mixture that is formed after the tests on the surface of LCP structure. Conceptually, it looks that LiOH/Li₂CO₃ mixture in molten state in the interface region of two-phase material promotes the proton conduction through LCP electrolyte, with negligible oxygen ion conduction.

Keywords La/Pr co-doped ceria (LCP) · Low-temperature ceramic fuel cell · Proton conduction · Two-phase material · LiOH/Li₂CO₃ mixture

1 Introduction

Solid oxide fuel cell (SOFC) and Protonic ceramic fuel cell (PCFC) have gained huge attention in the recent years for the direct use of chemical energy of fuels to generate electricity with high efficiency and low emission [1, 2]. According to the classification of transported carriers, ceramic fuel cell (CFC) includes SOFC, which is mainly oxygen ion conduction, and PCFC, which is mainly proton conduction. Conventional SOFC, realised by yttria stabilized zirconia (YSZ) that requires a high working temperature (800–1000 °C) to achieve sufficient ionic conductivity (> 0.1 S/cm) that is demanded for the device operation and it poses a huge challenge for its commercial application. Due to high temperature requirement, it increases the complexity of conventional technology, and ultimately raises the capital cost of the device [3, 4]. Goodenough introduced the concept of materials which could operate at sufficiently low temperatures below 700 °C [5]. In the field of low-temperature SOFC, well-studied doped zirconia electrolytes materials are replaced by gadolinium doped ceria (GDC) as well as samarium doped ceria (SDC) [6, 7]. Compared to the

✉ Fan Yang
yang_fan@seu.edu.cn

✉ Jung-Sik Kim
jskim@buaa.edu.cn

Xinlei Yang
brobow@163.com

Muhammad Afzal
afzalm@kth.se

Wanli Sun
s15378723296@163.com

¹ Jiangsu Provincial Key Laboratory of Solar Energy Science and Technology/Energy Storage Joint Research Center, School of Energy and Environment, Southeast University, Nanjing 210096, China

² Department of Energy Technology, KTH Royal Institute of Technology, 10044 Stockholm, SE, Sweden

³ Sino-French Engineer School/School of General Engineering, Beihang University, 37 Xueyuan Road, Haidian District, Beijing 100191, China

conventional YSZ based fuel cells, the ceria-based electrolytes show lower activation energy and therefore, can work at 400–700 °C [8, 9].

Meanwhile, as an alternative electrolyte of oxygen ion conductor, proton conductor ceramic materials have emerged as potential candidates. In this aspect, perovskite ceramic electrolytes with a high proton conductivity exhibit promising results in hydrogen or water vapor atmosphere. Generally, it is considered that Grothuss and Vehicle mechanisms are two main mechanisms of proton conductivity [10]. The former is due to the jumps of excess hydrogen through the bonds from one stationary lattice oxygen to the neighbouring lattice oxygen; the latter is due to the attachment of protons with the oxygen ions and then move in the form of OH⁻ ions via translational diffusion mechanism through appropriate vacancies in the perovskites [11]. Protons move easily through the lattice, which results in proton conduction being activated at lower activation energy level compare to that of attachment with oxygen ions and the composed conduction [7]. Here, BaZr_{0.8}Y_{0.2}O₃ (BZY) and BaCe_{0.7}Zr_{0.1}Y_{0.2}O_{3-δ} (BCZY) electrolytes are some typical examples for proton conduction [12, 13]. Compared to conventional SOFC, PCFC is composed of proton-conducting ceramic oxides and has greater potential for low-temperature operation [14]. Table 1 gives an overview of the electrochemical performance of PCFCs. As shown in Table 1, doped BaCeO₃ and doped BaZrO₃ electrolytes, which have been extensively investigated in recent years, exhibit a potential to operate at low temperatures (300–550 °C).

Usually, in ceria-based electrolytes, performance enhancement is achieved through doping of other elements. As an example, samarium doped ceria (SDC) where Sm³⁺ replacing Ce⁴⁺ in CeO₂, generates extra vacancies for oxygen and thereafter, oxygen ion conductivity increases through SDC as an electrolyte. In fact, the mechanism of changing overall conductivity of the electrolytes depend on the variation of different doping ratios. Sm, Gd, Y, La, Nd, and Pr are +3 valence ions, and are useful to generate more oxygen vacancies due to smaller enthalpy value of association and also the ionic compensation among Ce⁴⁺ and +3 valence ions [21]. Especially, in La and Pr co-doped ceria, we have come to know that larger radii of La³⁺ and Pr³⁺

ions lead towards the high lattice strain, that increases the defect formation in response [22]. Meanwhile, excess Pr³⁺ ions limit the carrier mobility and increase the band gap value, and the high band gap limits the formation of oxygen vacancies [23]. However, the doping of La³⁺ ions into the main ceria lattice results turning it into a donor level, which supports decrease in the band gap between valence and conduction bands and therefore, the phenomena counteracts to increase a possibility of oxygen vacancy formation [24].

Besides, this study is aimed to understand the conduction mechanism through La/Pr co-doped ceria (LCP) electrolyte for high-performance low-temperature CFC. In addition, LCP sample is sandwiched between two identical layers of Ni_{0.8}Co_{0.15}Al_{0.05}LiO_{2.8} (NCAL) coated Ni foam (NCAL-Ni) in order to construct a mechanically robust symmetric cell. Finally, the device is tested in fuel cell conditions; the cell has achieved a superior power density with a noticeably high ionic conductivity at sufficiently low temperature, i.e. @ 520 °C. Furthermore, the cell was examined for the gain mechanism of the NCAL-Ni/LCP/NCAL-Ni cell and proton conduction was found. This work demonstrates LCP electrolyte with novel proton conduction for developments of CFC, giving a new path for CFC development which could be practically possible at affordable temperatures.

2 Experimental

2.1 Materials Preparation

The original material used in this work is industrial-grade rare-earth LaCePr-carbonate purchased from Inner Mongolia Baotou Rare-Earth Hi-Tech Co Ltd, China. The LaCePr-carbonate is an industrial-grade mineral mainly composed of La₂(CO₃)₃ (24.9 wt%), Ce₂(CO₃)₃ (74.7 wt%), and Pr₂(CO₃)₃ (0.4 wt%), which is used as the raw material to produce industrial-grade rare-earth oxides. The electrode material NCAL is purchased from Tianjin Bamo Science & Technology Joint Stock Ltd., China. The LaCePr-carbonate is heat-treated at 800 °C for 4 h to get LCP for the subsequent experiments. Previous study has established that the LCP with the chemical formula La_{0.33}Ce_{0.62}Pr_{0.05}O_{2.8} [25–28].

Table 1 An overview of the maximum power density (MPD) of PCFCs at low temperature in the recent five years

Configuration	Temp. (°C)	MPD (mW/cm ²)	References
BZY20-Ni/BZY20/BCFZY0.1	500	455	[15]
Ni-BCZNY/BCZY/LSCF-BZCY	550	326	[16]
NiO-BCZYZn05/BCZYZn05/BSCF-BCZYZn05	550	278	[17]
NiO-BCZY/BCZYYb/BCFZY	550	500	[18]
Ni-BZCYYbN/BZCYYbN/BCCY	550	421	[19]
Ni-BZCYYbPd/BZCYYbPd/BCFZY	550	456	[20]

BCZY ($\text{BaCe}_{0.7}\text{Zr}_{0.1}\text{Y}_{0.2}\text{O}_{3-\delta}$) is synthesized using sol–gel method. $\text{Ba}(\text{NO}_3)_2$ (> 99%, purchased from Aladdin Bio-Chem Technology Ltd., China), $\text{Zr}(\text{NO}_3)_4 \cdot 5\text{H}_2\text{O}$ (99.99%, purchased from Macklin Biochemical Co., Ltd., China), $\text{Ce}(\text{NO}_3)_2 \cdot 6\text{H}_2\text{O}$, $\text{Y}(\text{NO}_3)_3 \cdot 6\text{H}_2\text{O}$ (purchased from A.R., Aladdin Bio-Chem Technology Ltd., China) were dissolved in ethylenediamine tetra acetic acid ($\text{C}_{10}\text{H}_{16}\text{N}_2\text{O}_8$, EDTA, purchased from A.R., Sinopharm Chemical Reagent Co., Ltd, China) solution according to the required stoichiometric ratio. Citric acid monohydrate ($\text{C}_6\text{H}_8\text{O}_7 \cdot \text{H}_2\text{O}$, purchased from A.R., Chron Chemicals Ltd., China) and $\text{C}_{10}\text{H}_{16}\text{N}_2\text{O}_8$ were added to the combined solution with a molar ratio of cation: citric acid: EDTA = 1: 1.5: 1. Then, ammonia solution ($\text{NH}_3 \cdot \text{H}_2\text{O}$, purchased from A.R., Sinopharm Chemical Reagent Co., Ltd., China) was used to adjust the solution with pH value to approximately 9, until the solution became transparent via a visual inspection. The resultant solution was continuously stirred at 120 °C for 4 h to evaporate the water to get grey colored gel after the auto-combustion. Finally, the gel was calcined at 1000 °C in air for 5 h to obtain final BZCY product.

2.2 Material Characterization

X-ray diffraction (XRD) of the powder samples was performed by an advanced X-ray diffractometer (Bruker D8 ADVANCE, Bruker Company, Germany) with Cu K α radiation ($\lambda = 1.54060 \text{ \AA}$). The morphology and detailed microstructure of the sample were studied using scanning electron microscopy (SEM; SU8010, Hitachi Limited, Japan) and high resolution transmission electron microscopy (TEM; Talos F200x, FEI Co., USA); also, an energy dispersive spectrometer (EDS) coupled with SEM focusing on O, Ce, La, and Pr elements was used to study the elemental composition. Valence state changes and different bonding mechanisms were detected by X-ray photoelectron spectroscopy (XPS; Escalab Xi+, Thermo Fischer Scientific, USA) in C 1s, O 1s, La 3d, Ce 3d and Pr 3d orbits. In addition, Fourier transform infrared spectroscopy (FTIR; Nicolet Is10, Thermo Fischer Scientific, USA) was performed to characterize the surface vibrational properties and the functional of the samples.

2.3 Fuel Cells Fabrication and Testing

The LCP fuel cells were fabricated via dry-pressing method. As show in Fig. S1, 0.2 g electrolyte powder was sandwiched between two pieces of NCAL-Ni electrodes by a unidirectional hydraulic press applying 10 MPa of compression to obtain a single cell with a configuration of NCAL-Ni/LCP/NCAL-Ni, which possessed an effective working area of 0.64 cm². Fig. S2 shows a cross-sectional SEM image of this cell, with a cell thickness of 2 mm and an electrolyte layer

thickness of 0.5 mm. H_2 with flow rate of 175 mL/min and pumped air with flow rate of 150 mL/min were utilized as fuel and oxidant, respectively. The *I-V* (current–voltage) and *I-P* (current–power) characteristics of the cell were measured at various temperatures using an IT8511 electronic load (ITECH Electrical Co., Ltd., China), while the data was recorded by an IT7000 software. An electrochemical workstation (CHI660E, ITECH Electrical Co., Ltd., China) was used to perform the electrochemical impedance spectroscopy (EIS), which was carried out at open circuit voltage from 1 MHz to 0.1 Hz with an amplitude of 5 mV.

3 Results and Discussion

3.1 Structural, Morphological and Compositional Analysis

Figure 1 shows XRD pattern of LCP that displays the same fluorite structure as that of CeO_2 (PDF No. 34–0394). The 2-theta value of the LCP peak is slightly shifted towards a lower angle as compared to that of pure CeO_2 . This can be considered as the doping effect of La^{3+} (1.16 Å) and Pr^{3+} (1.12 Å) with larger ionic radii instead of Ce^{4+} (0.97 Å), resulting in lattice expansion [29].

Figure 2(a) shows the SEM image of LCP, it can be observed that the industrial-grade rare-earth LCP material after direct sintering at 800 °C has an irregular particle structure with some agglomeration. The particle size distribution of LCP is measured between 100 and 300 nm. From the EDS images in Fig. 2(b–e), the main elements of

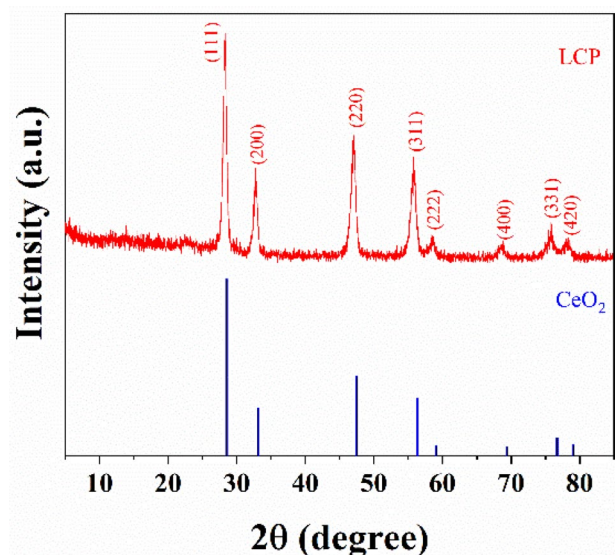


Fig. 1 XRD patterns of LCP electrolyte.

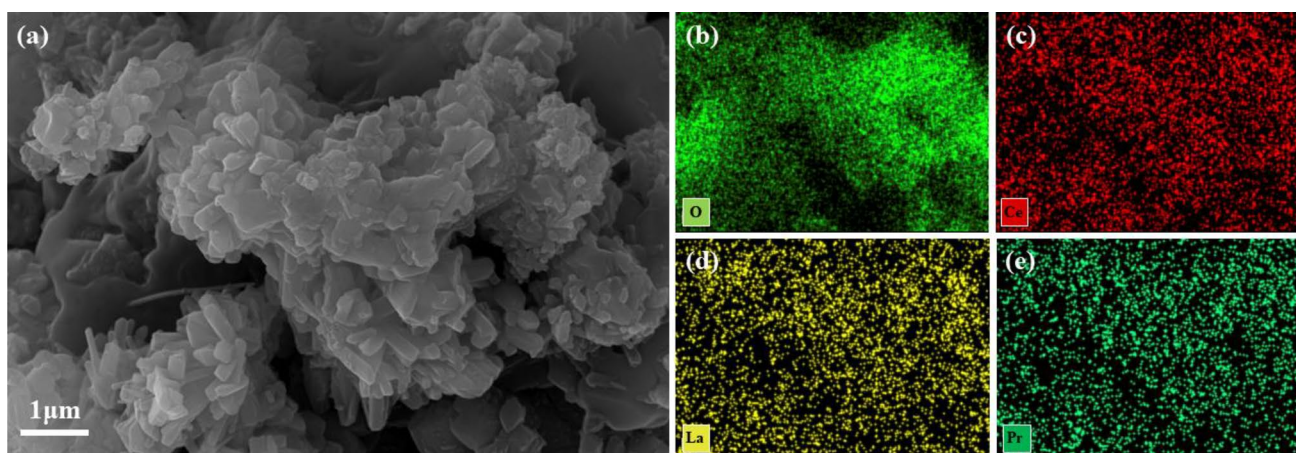


Fig. 2 a SEM image of LCP electrolyte, **b** O, **c** Ce, **d** La and **e** Pr EDS images for elemental mapping of the LCP electrolyte.

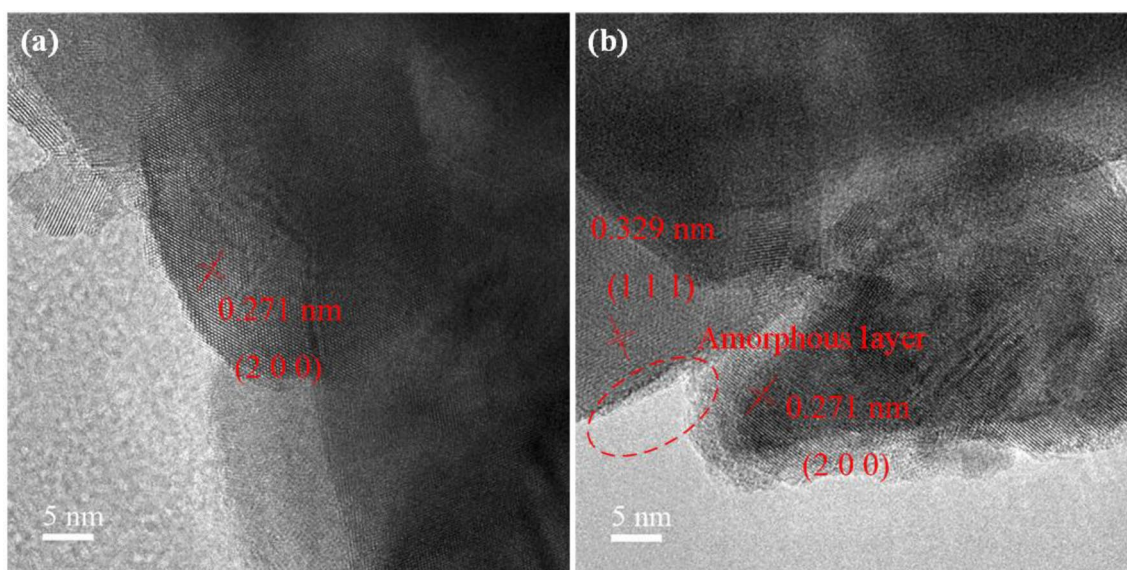


Fig. 3 TEM images of LCP electrolyte **a** before the testing and **b** after the testing.

LCP material are observed as uniformly distributed along the overall material structure.

Figure 3(a) and (b) show the TEM images of LCP with the lattice spacing of 0.271 nm and 0.329 nm in the (111) and (200) planes, respectively, which is larger than that of CeO_2 . Comparing the TEM images (a) before the testing and (b) after the testing, it can be observed that there is an amorphous layer (dotted area) on the surface of the LCP particles after the testing. The development of this amorphous layer after electrochemical testing has been easily detected in nanostructured fuel cells with NCAL electrode, due to the reductive NCAL materials in fuel gases environment together with the initial porous structure of electrolyte. The composition and detailed mechanism of this amorphous

layer would be revealed by the following XPS and FTIR analysis.

3.2 Electrochemical Performance of the Device and Conduction Mechanism

At different temperatures, Fig. 4(a) displays the I-V and I-P characteristics of the LCP electrolyte fuel cell. The LCP device has a MPD of 757 mW/cm^2 at 520°C , and its open circuit voltage (OCV) is 1.071 V. Observed OCV increases with a decrease in temperature, agreeing with the Nernst equation. Furthermore, this figure depicts the MPDs of 619, 552, 292, 153 and 30 mW/cm^2 at 500, 480, 460, 440 and 420°C . The sudden decrease of MPD observed when the

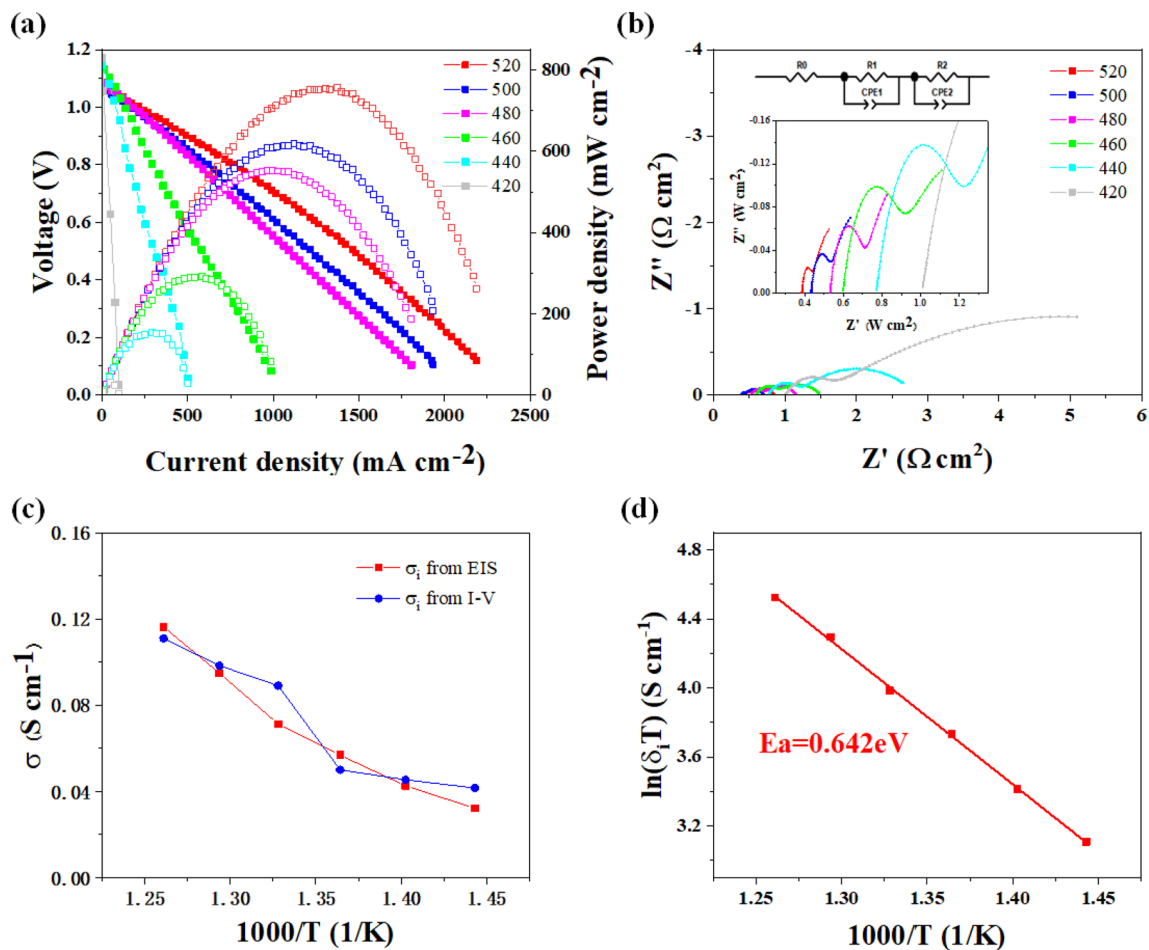


Fig. 4 **a** I-V and I-P characteristics of the LCP electrolyte fuel cell; **b** EIS of LCP electrolyte fuel cell tested under H₂/air conditions; **c** Conductivity plots and **d** Arrhenius plots of the LCP electrolyte fuel cell.

temperature was reduced to 420 °C can be explained by phase transition in the electrolyte. In the fuel cell test, the NCAL anode was reduced in hydrogen atmosphere forming LiOH/Li₂CO₃ mixture, which in molten state diffused into the electrolyte [30, 31]. In the preparation of NCAL-Ni electrode, NCAL powder was mixed with ethanol and terpineol solvent to get slurry and pasted on the Ni foam. Therefore, the ethanol and terpineol are believed to be the main source of the carbon in the amorphous layer. Besides, CO₂ in the air is also a possible source. In molten/partially molten states, LiOH/Li₂CO₃ mixture seals both the porous anode and the electrolyte, resulting in a high OCV that is saturated to the theoretical value [32]. Correspondingly, when the temperature decreases to 420 °C, the MPD of the cell deteriorated dramatically. In the study of NCAL/GDC/NCAL fuel cell, 419 °C was considered as the melting/solidification critical point of LiOH/Li₂CO₃ mixture [33]. As the LiOH/Li₂CO₃ mixture solidifies in the LCP device at around 419 °C, the conductivity of the electrolyte dropped abruptly disrupting a production of power output. In addition, the solidification

point of LiOH is 471 °C, and the sudden power density degradation at 460 °C may be caused by the partial solidification of LiOH in the LiOH/Li₂CO₃ mixture.

Figure 4(b) exhibits the EIS results for the LCP fuel cell in H₂/air atmosphere from 520 °C down to 420 °C. The raw data were fitted to the equivalent circuit by Zview. In the EIS, the x-axis intercept at high frequencies indicates the ohmic impedance, and similarly, the x-axis intercepts at medium and low frequencies indicate the charge transfer impedance and mass transfer impedance, respectively [34]. The Nyquist plot can be modeled using an equivalent circuit, where R_0 represents the bulk conduction resistance, R_1 represents the grain boundary conduction resistance, R_2 represents the electrode polarization resistance, and CPE is its corresponding constant element phase. Table 2 shows the results of the fitting calculation.

The ionic conductivity can be calculated by the following equation:

Table 2 The fitting parameters obtained from Zview with an equivalent circuit. The R and constant phase element (CPE) have the units of $\Omega \text{ cm}^2$ and F cm^{-2} , respectively

Temp	R_0	R_1	CPE1-T	CPE1-P	R_2	CPE2-T	CPE2-P
520 °C	0.386	0.043	0.017	0.889	0.280	1.466	0.546
500 °C	0.433	0.093	0.013	0.758	0.322	1.014	0.559
480 °C	0.531	0.169	0.006	0.747	0.457	0.722	0.564
460 °C	0.597	0.281	0.006	0.689	0.624	0.599	0.459
440 °C	0.769	0.402	0.005	0.683	1.691	0.581	0.434
420 °C	1.003	0.546	0.005	0.672	6.643	0.475	0.339

$$\sigma_i = \frac{L}{R \times S} \quad (1)$$

where L denotes the width of the electrolyte, S denotes the active area of the cell, and R denotes the resistance associated with the electrolyte. Here, R can be represented in two ways: 1. the value of $R_0 + R_1$ in the EIS results; 2. the resistance of the I-V curve in the ohmic polarization region [34].

As shown in Fig. 4(c), the ionic conductivity of LCP is 0.111–0.032 S/cm at 520–420 °C, which is significantly higher than that of conventional oxygen ion conductors. In this case, the result obtained by simulating the ohmic resistance in the EIS is the total conductivity influenced by ions and electrons. In contrast, the resistance of the linear part of the ohmic polarization region in the polarization curve corresponds to the ionic conductivity. The ionic conductivity (δ_i) results from the EIS are not significantly different from the polarization curve (I-V curve) obtained, and it can be judged that the electron conductivity in the LCP fuel cell is negligible Table 2.

The activation energy can be calculated by the following Arrhenius equation [35].

$$\ln(\sigma_i T) = \ln(A) - \frac{E_a}{R} \times \frac{1}{T} \quad (2)$$

Here, A is a pre-exponential factor, T is temperature in kelvin, R is the molar gas constant, and E_a is the activation energy of ion migration. As shown in Fig. 4(d), E_a obtained by EIS is 0.642 eV. Because of its high ionic conductivity and low activation energy, the LCP electrolyte cannot be a conventional oxygen ion conductor as they usually exhibit their activation energy greater than 1.0 eV, whilst the activation energy for surface conduction mechanism can be as

low as 0.2 eV [7, 36]. In order to elucidate the conduction mechanism of LCP electrolyte and the reason for its high performance, the investigation carried on further.

To investigate the type of carrier conduction in LCP material, BCZY was used as the blocking layer. BCZY exhibits proton conduction at low temperatures [13, 37]. This method is often used to determine the proton conductivity of electrolyte materials [28, 38]. Figure 5(a) shows the I-V and I-P characteristics of cell that is constructed using two 0.05 g BCZY blocking layers at each side of LCP electrolyte, as shown in Fig. 5(b). The cell has MPD of 732 mW/cm² at 520 °C with an OCV of 1.062 V. The comparison of MPD at 520 °C from this cell with that (757 mW/cm²) of a cell without the blocking layer in it indicates a marginal difference, proving that proton conduction dominates through a LCP electrolyte layer for low-temperature CFC.

In fuel cells, hydrogen bonding is considered as the pathway for proton conduction [39, 40]. In order to verify the proton conduction mechanism through a LCP electrolyte, FTIR (Fourier transform infrared spectroscopy) characterization was used to investigate any effect in the material before and after the cell's performance tests, as shown in Fig. 6. The peak at 3435 cm⁻¹ is the O-H bond in LiOH and H₂O, and the peak at 2922 cm⁻¹ is caused by the stretching vibration of O-H [41, 42]. These indicate that there are many OH groups in the LCP electrolyte and that protons may be transferred in the electrolyte in the form of O-H. Also, the peak at 2345 cm⁻¹ is caused by the O=C=O antisymmetric stretching vibration, the peaks at 1499 cm⁻¹ and 1439 cm⁻¹ are attributed to the antisymmetric stretching vibration of CO₃²⁻, and the peak at 864 cm⁻¹ is caused by the out-plane bending vibration of CO₃²⁻ [43, 44]. This may be an effect that is related to the infiltration of LiOH/Li₂CO₃ mixture in

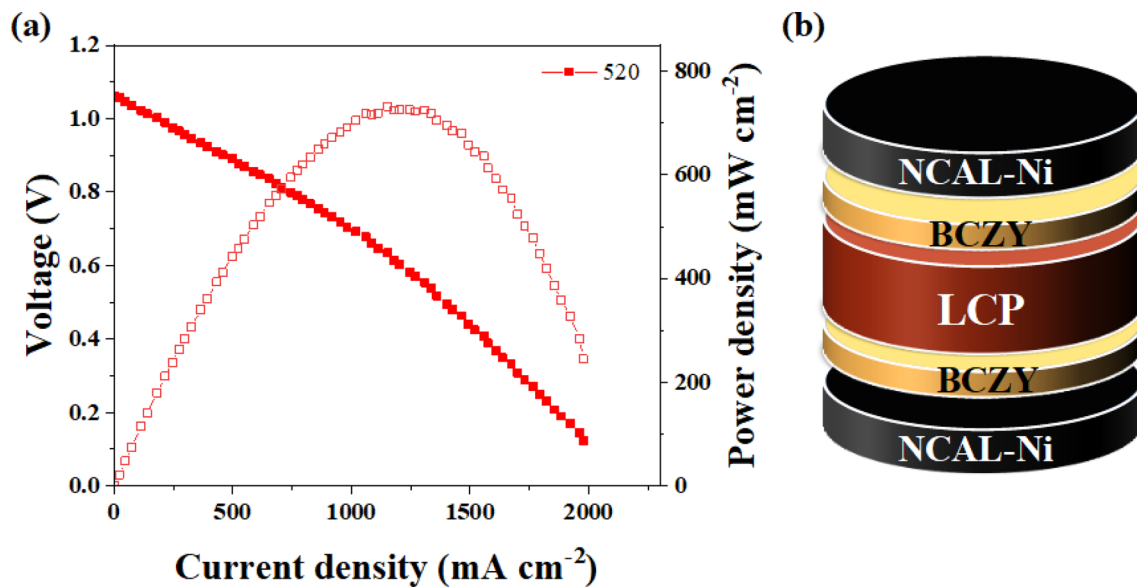


Fig. 5 **a** I-V and I-P characteristics of the NCAL-Ni/BCZY/LCP/BCZY/NCAL-Ni fuel cell measured at 520 °C and **b** the corresponding schematic of the cell structure.

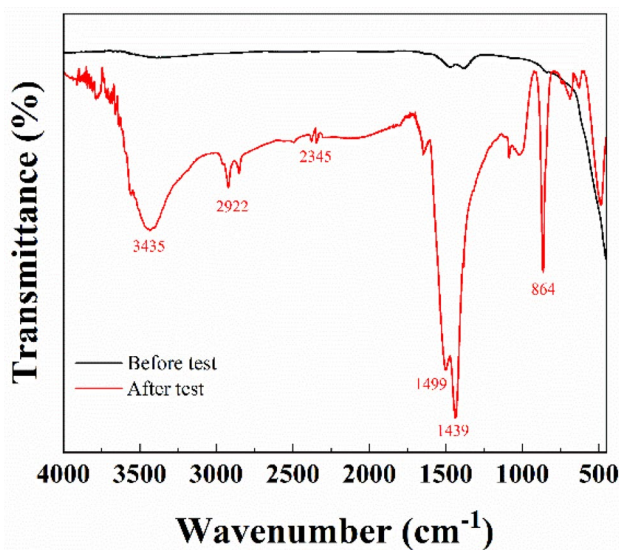


Fig. 6 FTIR spectra of the LCP cell before and after the test.

the NCAL electrode. The faint peaks at the same positions of 1499 cm^{-1} and 1439 cm^{-1} in the cell before the test may be caused by some residues of the LaCePr-carbonate.

For further surface analysis of LCP, the valence state changes of the material was investigated using XPS. As shown in Fig. 7(a), the main characteristic peaks of O, Ce, La and Pr can be found in a wide range of XPS spectra from simple LCP samples. In contrast, in the tested LCP cell, the characteristic peaks of Ce, La, and Pr are no longer detectable, while the faint characteristic peaks of Li elements can be detected. In Fig. 7(b), the XPS spectra of C 1 s before

the test and after the test can be fitted into two peaks. Position 1 (298.21 eV) and 1' (298.77 eV) can be assigned to the CO_3^{2-} , position 2 (284.83 eV) and 2' (284.76 eV) can be assigned to the hydrocarbon [33]. In Fig. 7(c), the peaks of adsorbed oxygen, associated with OH^- , CO_3^{2-} and oxygen vacancies, with binding energy around position 1 (531.35 eV) and 1' (531.55 eV) appears in the O 1 s XPS spectrum, while position 2 (528.54 eV) is attributed to lattice oxygen [33, 45]. It is noticeable that the peaks indicating OH^- and CO_3^{2-} are significantly enhanced after the test, while the peaks of lattice oxygen are almost difficult to be detected. This indicates that during the fuel cell testing, the NCAL anode was reduced under hydrogen environment and formed $\text{LiOH}/\text{Li}_2\text{CO}_3$ mixture in the molten state [32]. The $\text{LiOH}/\text{Li}_2\text{CO}_3$ mixture diffuse into the electrolyte and is filled between the interfaces of the LCP particles forming an amorphous layer, as shown in Fig. 3(b). This amorphous layer has been reported in previous nanostructured LST, BCY and GDC fuel cells using the same dry-pressing method similar in LCP too [32, 33, 42, 46]. The authors speculate that this amorphous layer forms a high-speed pathway for ion conduction on the surface of LCP particles, which helps to enhance the proton conductivity of LCP electrolyte and hence improve the power output of the cell.

Recently, proton conduction is reported at the interface of nanostructured oxides and carbonates [47]. Ricca et al. suggested that LiKCO_3 is coated on the surface of YSZ, forming a high-speed pathway for ion transport in the two-phase interface region [48]. Wang et al. investigated the $\text{SDC}/\text{Na}_2\text{CO}_3$ nanocomposite electrolyte and concluded that the interface due to the introduction of carbonate enhances

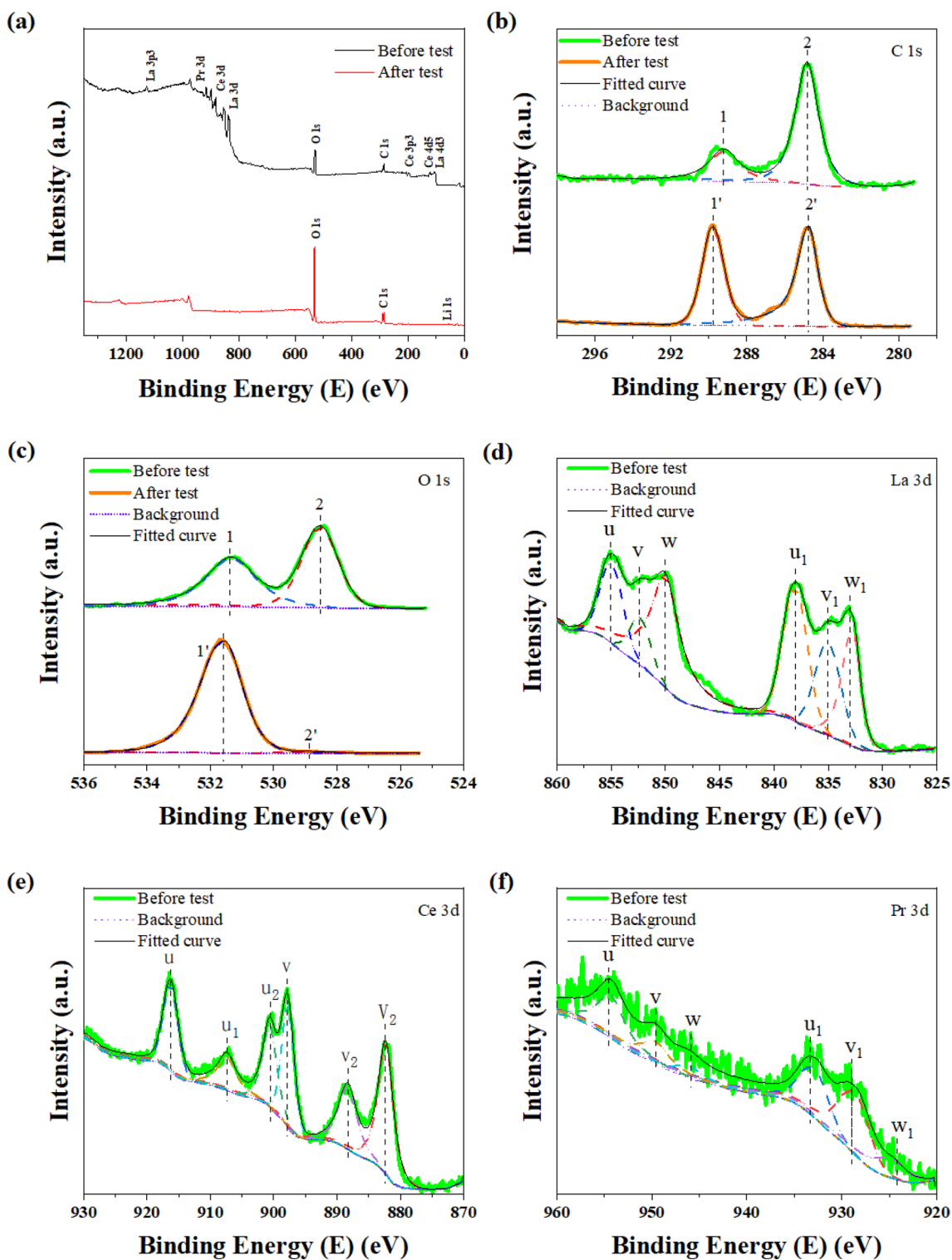


Fig. 7 XPS spectra of (a) the wide survey of all elements; b C 1s, c O 1s, d La 3d e Ce 3d and f Pr 3d of LCP.

the proton conduction and used a “Swing Model”. In their model, protons form meta-stable hydrogen bonds with oxygen ions from both CO_3^{2-} group and the surface of SDC as a conduction pathway [49]. Similarly, in the LCP electrolyte, the $\text{LiOH/Li}_2\text{CO}_3$ mixture coated on the surface of LCP particles establishes a high-speed pathway for proton transfer. The bending and stretching vibrations of CO_3^{2-} demonstrate the process of hydrogen bond formation and breaking between proton and CO_3^{2-} groups. Along the direction of hydrogen concentration, the $\text{H}^+\text{-CO}_3^{2-}$ bond becomes one of the main pathways for proton conduction. Moreover, O–H stretching vibration was also observed, which may be caused by hydrogen bond between protons and oxygen atoms on the LCP surface. The concentration difference cell method was used to investigate the LCP ion conduction mechanism without the influence of $\text{LiOH/Li}_2\text{CO}_3$ mixture. The concentration cell method is often used to determine the carrier type and a number of ion transfer within fuel cells [50]. For instance, $\text{LiAl}_{0.5}\text{Co}_{0.5}\text{O}_2$, BCY and other materials demonstrated the conduction mechanism using same method [46, 51]. Hydrogen concentration cells (HCC) were fabricated using platinum as the symmetric electrode and oxygen concentration cells (OCC) were fabricated using silver as the symmetric electrode. The voltage of HCC was recorded under the conditions of $5\%\text{H}_2 + 95\%\text{Ar}$ and pure H_2 on one and other side of the cell [52]. The voltage of the OCC was recorded under the conditions of $2\%\text{O}_2 + 98\%\text{Ar}$ and $21\%\text{O}_2 + 79\%\text{N}_2$ on one and other side of the cell. The theoretical voltage value of concentration cell was calculated by Eq. (3), where p_1 and p_2 are the partial pressures of fuel on each side of the cell, respectively, and n is the number of transferred electrons. The transfer number of protons and O^{2-} can be calculated by Eq. (4), based on the measured voltage E_{obs} and the theoretical voltage E_{Nernst} .

$$E_{\text{Nernst}} = \frac{RT}{nF} \ln\left(\frac{p_1}{p_2}\right) \quad (3)$$

$$t_{\text{ion}} = \frac{E_{\text{obs}}}{E_{\text{Nernst}}} \quad (4)$$

The proton transfer number of HCC shown in Fig. 8(a) is 42.8%–63.5% at 400–550 °C. As shown in Fig. 8(b), the oxygen ion transfer number of OCC is 16.9%–27.1%. This result indicates that proton conduction dominates in pure LCP with the presence of oxygen ion conduction. In the results of Fig. 6, the O–H stretching vibration peak at 2922 cm^{-1} in the NCAL-Ni/LCP/NCAL-Ni cell indicates that the proton conduction may be through the formation of O–H bonds between protons and oxygen atoms on the LCP surface. It is also one of the main pathways of proton conduction in the similar Grotthuss model. Figure 7(d–f) show that in LCP before the test, Ce element is mainly present at +4 valence, La element is mainly present at +3 valence, while Pr element is present at both +3 and +4 valence. In the fluorite structure of ceria-based materials, Ce^{4+} is doped by La^{3+} and $\text{Pr}^{3+}/\text{Pr}^{4+}$ in high proportion, forming many oxygen vacancies. These oxygen vacancies provide a conduction pathway for O^{2-} . However, the low oxygen ion transfer number is due to the effect of low temperature below 550 °C on the one hand, and on the other hand, the doping of rare-earth cations with large radii such as La^{3+} and Pr^{3+} make the formed oxygen vacancies unstable as revealed by the study of Nakayama et al. using the first principle [53]. In fuel cell conditions, both H^+ and O^{2-} can be sourced externally from hydrogen and oxygen. In contrast, in HCC or OCC tests, different gas atmospheres will result in different ion conduction mechanisms with the fuel cell atmosphere [54].

According to the combined analysis, the authors have proposed the conduction mechanism in NCAL-Ni/LCP/NCAL-Ni fuel cell, as shown in Fig. 9. During the cell operation,

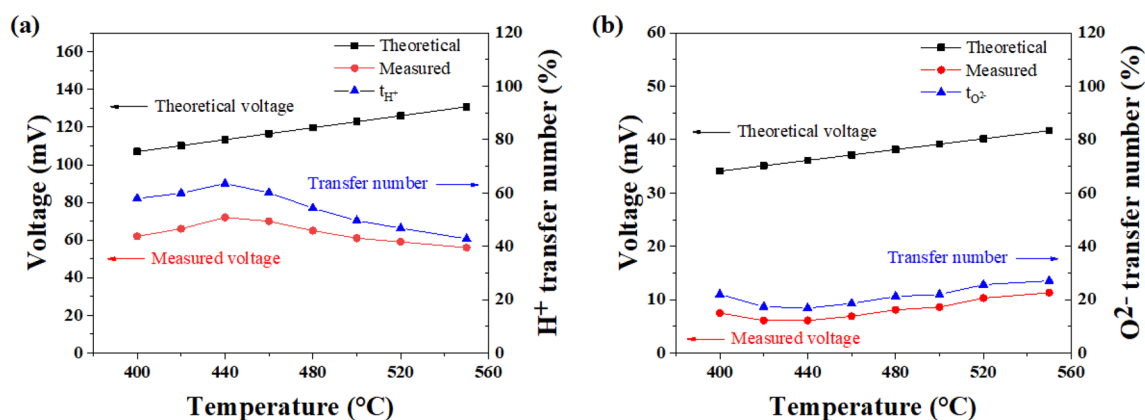
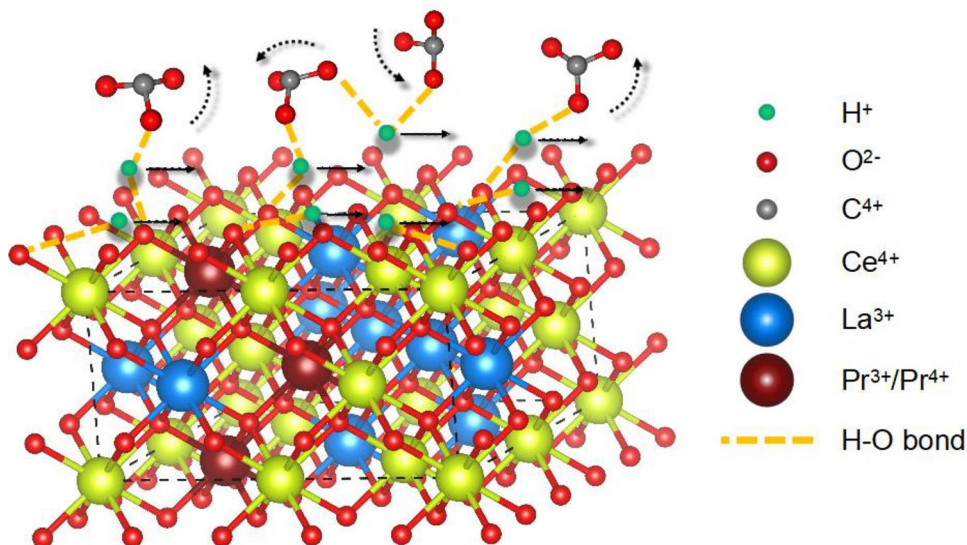


Fig. 8 The observed OCV, theoretical OCV, and transfer number from (a) hydrogen concentration cell and (b) oxygen concentration cell.

Fig. 9 Conduction mechanism in NCAL-Ni/LCP/NCAL-Ni fuel cell.



the $\text{LiOH}/\text{Li}_2\text{CO}_3$ mixture in molten or partially molten state is automatically coated on the surface of the LCP particles forming a core-shell structure [55]. The proton has a smaller radius and lighter mass and is believed to form a hydrogen bond with the neighboring lattice O atom [56]. In the two-phase interfacial region, proton conduction takes place mainly in two ways: 1. H–O bonds are formed among protons and oxygen atoms of CO_3 group; 2. H–O bonds are formed among protons and oxygen atoms on the LCP surface. These H–O bonds are continuously forming and breaking, allowing proton conduction along this high-speed pathway in the direction of hydrogen concentration. On one hand, the rotational motion of the CO_3 group enables the proton to pass across the CO_3 groups through the H–O bond. On the other hand, proton passes from one oxygen atom to another one on the surface of the LCP particles via the H–O bond. The stretching and bending vibrations of CO_3^{2-} and the stretching vibrations of O–H demonstrate these processes. Expectedly, the protons may form both H–O bonds to the CO_3 group and the oxygen atom on LCP surface. In this case, the rotating CO_3 group may promote the transfer of protons across the oxygen atoms on the LCP surface. For the LCP electrolyte with low oxygen ion conduction, when NCAL is used as the electrode, the $\text{LiOH}/\text{Li}_2\text{CO}_3$ mixture formed by the reduction of the anode greatly promotes the proton conduction, making the contribution of O^{2-} in the NCAL-Ni/LCP/NCAL-Ni fuel cell almost negligible. In addition, the molten constituent covers the surface of LCP particles, which may hinder the internal electron conduction through the bulk electrolyte and can help to avoid internal short circuit [31].

4 Conclusions

LCP based low-temperature CFC using NCAL as the electrodes, has achieved a peak power density more than $750 \text{ mW}/\text{cm}^2$ at $520 \text{ }^\circ\text{C}$. Adding BCZY blocking layer helps to demonstrate that the NCAL-Ni/LCP/NCAL-Ni cell to become dominated with proton conduction. In the molten state $\text{LiOH}/\text{Li}_2\text{CO}_3$ mixture on the surface of LCP particles, protons form H–O bonds with oxygen atoms in CO_3 groups and meanwhile form H–O bonds with oxygen atoms on the surface of LCP, establishing a high-speed pathway for proton transfer. The high-speed pathway at the interface between the LCP particles and the $\text{LiOH}/\text{Li}_2\text{CO}_3$ mixture has a great influence on the enhancement of the ionic conductivity. It was demonstrated via HCC/OCC tests that the LCP electrolyte is a mixed conductor with proton and O^{2-} when there is no $\text{LiOH}/\text{Li}_2\text{CO}_3$ mixture produced by the NCAL electrode. $\text{LiOH}/\text{Li}_2\text{CO}_3$ mixture promoted the proton conduction through an LCP electrolyte layer to a promising level that oxygen ion conduction was almost negligible through the NCAL-Ni/LCP/NCAL-Ni device.

Supplementary Information The online version contains supplementary material available at <https://doi.org/10.1007/s40684-023-00532-5>.

Acknowledgements This work was supported by the Fundamental Research Funds for the Central Universities (Grant No.3203002205A1 and 4003002204) and Jiangsu Provincial program (Project No. JSSCRC2021491).

Data availability The data that support the findings of this study are available on request from the corresponding author.

Declarations

Conflict of interest On behalf of all authors, the corresponding author states that there is no conflict of interest.

References

- Boldrin, P., & Brandon, N. P. (2019). Progress and outlook for solid oxide fuel cells for transportation applications. *Nature Catalysis*, 2(7), 571–577. <https://doi.org/10.1038/s41929-019-0310-y>
- Lu, Y., Zhu, B., Shi, J., & Yun, S. (2021). Advanced low-temperature solid oxide fuel cells based on a built-in electric field. *Energy Materials*, 1, 100007. <https://doi.org/10.20517/energymater.2021.06>
- Wachsman, E. D., & Lee, K. T. (2011). Lowering the temperature of solid oxide fuel cells. *Science*. <https://doi.org/10.1126/science.1204090>
- Shao, Z., Zhou, W., & Zhu, Z. (2012). Advanced synthesis of materials for intermediate-temperature solid oxide fuel cells. *Progress in Materials Science*. <https://doi.org/10.1016/j.pmatsci.2011.08.002>
- Goodenough, J. B. (2000). Oxide-ion conductors by design. *Nature*, 404(6780), 821–823. <https://doi.org/10.1038/35009177>
- Zhang, S., Liu, T., Li, C., Yao, S., Li, C., Yang, G., & Liu, M. (2015). Atmospheric plasma-sprayed $\text{La}_{0.8}\text{Sr}_{0.2}\text{Ga}_{0.8}\text{Mg}_{0.2}\text{O}_3$ electrolyte membranes for intermediate-temperature solid oxide fuel cells. *Journal of Materials Chemistry A*. <https://doi.org/10.1039/C5TA01203A>
- Arunkumar, P., Meena, M., & Babu, K. S. (2012). A review on cerium oxide-based electrolytes for ITSOFC. *Nanomaterials and Energy*, 1(5), 288–305. <https://doi.org/10.1680/nme.12.00015>
- Fabbri, E., Pergolesi, D., & Traversa, E. (2010). Materials challenges toward proton-conducting oxide fuel cells: A critical review. *Chemical Society reviews*, 39(11), 4355–4369. <https://doi.org/10.1039/b902343g>
- Zhu, B., Mi, Y., Xia, C., Wang, B., Kim, J. S., Lund, P., & Li, T. (2021). Nano-scale view into solid oxide fuel cell and semi-conductor membrane fuel cell material and technology. *Energy Materials*. <https://doi.org/10.20517/energymater.2021.03>
- Wang, H., Wang, X., Meng, B., Tan, X., Loh, K. S., Sunarso, J., & Liu, S. (2018). Perovskite-based mixed protonic–electronic conducting membranes for hydrogen separation: recent status and advances. *Journal of Industrial and Engineering Chemistry*, 60, 297–306. <https://doi.org/10.1016/j.jiec.2017.11.016>
- Ni, M., & Shao, Z. (2020). Fuel cells that operate at 300° to 500°C. *Science*. <https://doi.org/10.1126/science.abc9136>
- Fabbri, E., Bi, L., Pergolesi, D., & Traversa, E. (2012). Towards the next generation of solid oxide fuel cells operating below 600 °C with chemically stable proton-conducting electrolytes. *Advanced Materials*. <https://doi.org/10.1002/adma.201103102>
- Zuo, C., Zha, S., Liu, M., Hatano, M., & Uchiyama, M. (2006). $\text{Ba}(\text{Zr}_{0.1}\text{Ce}_{0.7}\text{Y}_{0.2})\text{O}_{3-\delta}$ as an electrolyte for low-temperature solid-oxide fuel cells. *Advanced Materials*. <https://doi.org/10.1002/adma.200601366>
- Cao, J., Ji, Y., & Shao, Z. (2022). Perovskites for protonic ceramic fuel cells: a review. *Energy & Environmental Science*, 15(6), 2200–2232. <https://doi.org/10.1039/D2EE00132B>
- Duan, C., Tong, J., Shang, M., Nikodemski, S., Sanders, M., Ricote, S., Almansoori, A., & O’Hayre, R. (2015). Readily processed protonic ceramic fuel cells with high performance at low temperatures. *Science*. <https://doi.org/10.1126/science.aab3987>
- Liu, Z., Zhou, M., Chen, M., Cao, D., Shao, J., Liu, M., & Liu, J. (2020). A high-performance intermediate-to-low temperature protonic ceramic fuel cell with in-situ exsolved nickel nanoparticles in the anode. *Ceramics International*. <https://doi.org/10.1016/j.ceramint.2020.05.062>
- Azad, A. K., Abdalla, A. M., Afif, A., Azad, A., Afroze, S., Idris, A. C., Park, J.-Y., Saqib, M., Radenahmad, N., Hossain, S., Elius, I. B., Al-Mamun, M., Zaini, J., Al-Hinai, A., Reza, M. S., & Irvine, J. T. S. (2021). Improved mechanical strength, proton conductivity and power density in an ‘all-protonic’ ceramic fuel cell at intermediate temperature. *Scientific Reports*, 11(1), 19382. <https://doi.org/10.1038/s41598-021-98987-6>
- Le, L. Q., Hernandez, C. H., Rodriguez, M. H., Zhu, L., Duan, C., Ding, H., O’Hayre, R. P., & Sullivan, N. P. (2021). Proton-conducting ceramic fuel cells: Scale up and stack integration. *Journal of Power Sources*. <https://doi.org/10.1016/j.jpowsour.2020.228868>
- Song, Y., Chen, J., Yang, M., Xu, M., Liu, D., Liang, M., Wang, Y., Ran, R., Wang, W., Ciucci, F., & Shao, Z. (2022). Realizing simultaneous detrimental reactions suppression and multiple benefits generation from nickel doping toward improved protonic ceramic fuel cell performance. *Small (Weinheim an der Bergstrasse, Germany)*, 18(16), e2200450. <https://doi.org/10.1002/sml.202200450>
- He, F., Gao, Q., Liu, Z., Yang, M., Ran, R., Yang, G., Wang, W., Zhou, W., & Shao, Z. (2021). A New Pd doped proton conducting perovskite oxide with multiple functionalities for efficient and stable power generation from ammonia at reduced temperatures. *Advanced Energy Materials*, 11(19), 2003916. <https://doi.org/10.1002/aenm.202003916>
- Bhabu, K. A., Theerthagiri, J., Madhavan, J., Balu, T., Rajasekaran, T. R., & Arof, A. K. (2016). Investigations on acceptor (Pr^{3+}) and donor (Nb^{5+}) doped cerium oxide for the suitability of solid oxide fuel cell electrolytes. *Ionics*, 22(12), 2461–2470. <https://doi.org/10.1007/s11581-016-1780-4>
- Ajith Kumar, S., Kuppusami, P., Amirthapandian, S., & Fu, Y.-P. (2020). Effect of Sm co-doping on structural, mechanical and electrical properties of Gd doped ceria solid electrolytes for intermediate temperature solid oxide fuel cells. *International Journal of Hydrogen Energy*, 45(54), 29690–29704. <https://doi.org/10.1016/j.ijhydene.2019.10.098>
- Kalpana Devi, A., Ram Kumar, G., Prerna, C., Amarsingh Bhabu, K., Sabarinathan, V., & Rajasekaran, T. R. (2020). Superiorly conductive La^{3+} and Pr^{3+} Co-doped cerium oxide for IT-SOFC applications. *Journal of Materials Science: Materials in Electronics*, 31(13), 10628–10638. <https://doi.org/10.1007/s10854-020-03612-3>
- Amarsingh Bhabu, K., Theerthagiri, J., Madhavan, J., Balu, T., & Rajasekaran, T. R. (2016). Superior oxide ion conductivity of novel acceptor doped cerium oxide electrolytes for intermediate-temperature solid oxide fuel cell applications. *The Journal of Physical Chemistry C*, 120(33), 18452–18461. <https://doi.org/10.1021/acs.jpcc.6b05873>
- Zhu, B., Liu, X., Zhu, Z., & Ljungberg, R. (2008). Solid oxide fuel cell (SOFC) using industrial grade mixed rare-earth oxide electrolytes. *International Journal of Hydrogen Energy*, 33(13), 3385–3392. <https://doi.org/10.1016/j.ijhydene.2008.03.065>
- Xia, C., Wang, B., Ma, Y.-Y., Cai, Y., Afzal, M., Liu, Y., He, Y., Zhang, W., Dong, W., Li, J., & Zhu, B. (2016). Industrial-grade rare-earth and perovskite oxide for high-performance electrolyte layer-free fuel cell. *Journal of Power Sources*, 307, 270–279. <https://doi.org/10.1016/j.jpowsour.2015.12.086>
- Xia, C., Wang, B., Cai, Y., Zhang, W., Afzal, M., & Zhu, B. (2017). Electrochemical properties of LaCePr -oxide/ K_2WO_4 composite electrolyte for low-temperature SOFCs. *Electrochemistry Communications*. <https://doi.org/10.1016/j.elecom.2016.12.013>

28. Qiao, Z., Xia, C., Cai, Y., Afzal, M., Wang, H., Qiao, J., & Zhu, B. (2018). Electrochemical and electrical properties of doped CeO₂-ZnO composite for low-temperature solid oxide fuel cell applications. *Journal of Power Sources*, 392, 33–40. <https://doi.org/10.1016/j.jpowsour.2018.04.096>
29. Jiang, Y., Huang, H., Wang, M., Zhang, W., & Wang, B. (2020). The influence of preparation pressure on the electrochemical performance of semiconductor-ionic membrane fuel cells (SIMFC). *Journal of Materials Science: Materials in Electronics*, 31(8), 6233–6240. <https://doi.org/10.1007/s10854-020-03177-1>
30. Zhou, J., Chen, G., Chen, Z., Wei, K., Guan, G., Geng, S., & Abudula, A. (2022). Effects of different lithium compound electrodes on the electrochemical performance of the ceramic fuel cells. *International Journal of Hydrogen Energy*, 47(86), 36640–36649. <https://doi.org/10.1016/j.ijhydene.2022.08.222>
31. Wei, K., Chen, G., Chen, Z., Dai, R., Yu, K., & Geng, S. (2022). Ionic conduction of ceramic/molten salt composite electrolyte in fuel cell with lithium compound as electrode. *Journal of The Electrochemical Society*. <https://doi.org/10.1149/1945-7111/ac908a>
32. Chen, Z., Chen, G., Zhang, R., Dai, R., Lv, X., & Geng, S. (2021). Toward understanding of temperature dependence of an advanced ceramic fuel cell with Ni_{0.8}Co_{0.15}Al_{0.05}LiO₂ as an electrode. *ACS Applied Energy Materials*, 4(8), 8386–8394. <https://doi.org/10.1021/acsaem.1c01613>
33. Zhang, R., Chen, G., Chen, Z., Dai, R., Lv, X., Lou, T., Li, Y., & Geng, S. (2021). Investigation of the sudden drop of electrolyte conductivity at low temperature in ceramic fuel cell with Ni_{0.8}Co_{0.15}Al_{0.05}LiO₂ electrode. *International Journal of Hydrogen Energy*, 46(54), 27793–27800. <https://doi.org/10.1016/j.ijhydene.2021.06.017>
34. Shah, M. A. K. Y., Lu, Y., Mushtaq, N., Singh, M., Rauf, S., Yousaf, M., & Zhu, B. (2022). ZnO/MgZnO heterostructure membrane with type II band alignment for ceramic fuel cells. *Energy Materials*. <https://doi.org/10.2057/energymater.2022.27>
35. Ali, A., Rafique, A., Kaleemullah, M., Abbas, G., Ajmal Khan, M., Ahmad, M. A., & Raza, R. (2018). Effect of alkali carbonates (single, binary, and ternary) on doped ceria: a composite electrolyte for low-temperature solid oxide fuel cells. *ACS Applied Materials & Interfaces*, 10(1), 806–818. <https://doi.org/10.1021/acsaami.7b17010>
36. Zhu, B., Li, S., & Mellander, B. E. (2008). Theoretical approach on ceria-based two-phase electrolytes for low temperature (300–600 °C) solid oxide fuel cells. *Electrochemistry Communications*, 10(2), 302–305. <https://doi.org/10.1016/j.elecom.2007.11.037>
37. Yang, L., Wang, S., Blinn, K. S., Liu, M., Liu, Z., Cheng, Z., & Liu, M. (2009). Enhanced sulfur and coking tolerance of a mixed ion conductor for SOFCs: BaZr_{0.1}Ce_{0.7}Y_{0.2-x}Yb_xO_{3-δ}. *Science*. <https://doi.org/10.1126/science.1174811>
38. Liu, J., Yang, F., Jiang, Z., Zhang, Y., Hu, E., Wang, H., & Yang, X. (2021). enhanced ionic conductivity and durability of novel solid oxide fuel cells by constructing a heterojunction based on transition and rare earth metal co-doped ceria. *ACS Applied Energy Materials*, 4(12), 13492–13503. <https://doi.org/10.1021/acsaem.1c01873>
39. Kreuer, K.-D., Paddison, S. J., Spohr, E., & Schuster, M. (2004). Transport in proton conductors for fuel-cell applications: simulations, elementary reactions, and phenomenology. *Chemical Reviews*, 104(10), 4637–4678. <https://doi.org/10.1021/cr020715f>
40. Kreuer, K.-D. (1996). Proton conductivity: materials and applications. *Chemistry of Materials*, 8(3), 610–641. <https://doi.org/10.1021/cm950192a>
41. Li, G. J., & Kawi, S. (1998). Synthesis, characterization and sensing application of novel semiconductor oxides. *Talanta*, 45(4), 759–766. [https://doi.org/10.1016/S0039-9140\(97\)00295-6](https://doi.org/10.1016/S0039-9140(97)00295-6)
42. Chen, G., Zhu, B., Deng, H., Luo, Y., Sun, W., Liu, H., Zhang, W., Wang, X., Qian, Y., Hu, X., Geng, S., & Kim, J. S. (2018). Advanced fuel cell based on Perovskite La-SrTiO₃ semiconductor as the electrolyte with superoxide-ion conduction. *ACS Applied Materials & Interfaces*, 10(39), 33179–33186. <https://doi.org/10.1021/acsaami.8b10087>
43. Chen, W. C., Lin, R. C., Tseng, S. M., & Kuo, S. W. (2018). Minimizing the strong screening effect of polyhedral oligomeric silsesquioxane nanoparticles in hydrogen-bonded random copolymers. *Polymers (Basel)*. <https://doi.org/10.3390/polym10030303>
44. Zheng, X., Li, X., Wang, Z., Guo, H., Huang, Z., Yan, G., & Wang, D. (2016). Investigation and improvement on the electrochemical performance and storage characteristics of LiNiO₂-based materials for lithium ion battery. *Electrochimica Acta*, 191, 832–840. <https://doi.org/10.1016/j.electacta.2016.01.142>
45. Zhang, W., Zhang, L., Guan, K., Zhang, X., Meng, J., Wang, H., Liu, X., & Meng, J. (2020). Effective promotion of oxygen reduction activity by rare earth doping in simple perovskite cathodes for intermediate-temperature solid oxide fuel cells. *Journal of Power Sources*. <https://doi.org/10.1016/j.jpowsour.2019.227360>
46. Chen, G., Zhang, X., Luo, Y., He, Y., Liu, H., Geng, S., Yu, K., & Dong, Y. (2020). Ionic conduction mechanism of a nanostructured BCY electrolyte for low-temperature SOFC. *International Journal of Hydrogen Energy*, 45(45), 24108–24115. <https://doi.org/10.1016/j.ijhydene.2019.07.223>
47. Lyu, Y., Xie, J., Wang, D., & Wang, J. (2020). Review of cell performance in solid oxide fuel cells. *Journal of Materials Science*, 55(17), 7184–7207. <https://doi.org/10.1007/s10853-020-04497-7>
48. Ricca, C., Ringuedé, A., Cassir, M., Adamo, C., & Labat, F. (2018). Conduction mechanisms in oxide-carbonate electrolytes for SOFC: highlighting the role of the interface from first-principles modeling. *The Journal of Physical Chemistry C*, 122(18), 10067–10077. <https://doi.org/10.1021/acs.jpcc.8b02174>
49. Wang, X., Ma, Y., Li, S., Kashyout, A.-H., Zhu, B., & Muhammed, M. (2011). Ceria-based nanocomposite with simultaneous proton and oxygen ion conductivity for low-temperature solid oxide fuel cells. *Journal of Power Sources*, 196(5), 2754–2758. <https://doi.org/10.1016/j.jpowsour.2010.11.033>
50. Pérez-Coll, D., Heras-Juaristi, G., Fagg, D. P., & Mather, G. C. (2014). Transport-number determination of a protonic ceramic electrolyte membrane via electrode-polarisation correction with the Gorelov method. *Journal of Power Sources*, 245, 445–455. <https://doi.org/10.1016/j.jpowsour.2013.06.155>
51. Lan, R., & Tao, S. (2014). Novel proton conductors in the Layered oxide material Li₁Al_{0.5}Co_{0.5}O₂. *Advanced Energy Materials*. <https://doi.org/10.1002/aenm.201301683>
52. Zhu, B., & Mellander, B. E. (1997). Proton conduction and diffusion in Li₂SO₄. *Solid State Ionics*, 97(1), 535–540. [https://doi.org/10.1016/S0167-2738\(97\)00057-X](https://doi.org/10.1016/S0167-2738(97)00057-X)
53. Nakayama, M., & Martin, M. (2009). First-principles study on defect chemistry and migration of oxide ions in ceria doped with rare-earth cations. *Physical Chemistry Chemical Physics*, 11(17), 3241–3249. <https://doi.org/10.1039/B900162J>
54. Fan, L., Wang, C., Chen, M., & Zhu, B. (2013). Recent development of ceria-based (nano)composite materials for low temperature ceramic fuel cells and electrolyte-free fuel cells. *Journal of Power Sources*. <https://doi.org/10.1016/j.jpowsour.2013.01.138>
55. Xing, Y., Wu, Y., Li, L., Shi, Q., Shi, J., Yun, S., Akbar, M., Wang, B., Kim, J.-S., & Zhu, B. (2019). Proton shuttles in CeO₂/CeO_{2-δ}

core-shell structure. *ACS Energy Letters*, 4(11), 2601–2607. <https://doi.org/10.1021/acseenergylett.9b01829>

56. Radenahmad, N., Afif, A., Petra, P. I., Rahman, S. M. H., Eriksson, S.-G., & Azad, A. K. (2016). Proton-conducting electrolytes for direct methanol and direct urea fuel cells – a state-of-the-art review. *Renewable and Sustainable Energy Reviews*, 57, 1347–1358. <https://doi.org/10.1016/j.rser.2015.12.103>

Publisher's Note Springer Nature remains neutral with regard to jurisdictional claims in published maps and institutional affiliations.

Springer Nature or its licensor (e.g. a society or other partner) holds exclusive rights to this article under a publishing agreement with the author(s) or other rightsholder(s); author self-archiving of the accepted manuscript version of this article is solely governed by the terms of such publishing agreement and applicable law.



Xinlei Yang Xinlei Yang is a master candidate in School of Energy and Environment at Southeast University. His current research interests are solid oxide fuel cells and semiconductor-ionic fuel cell.

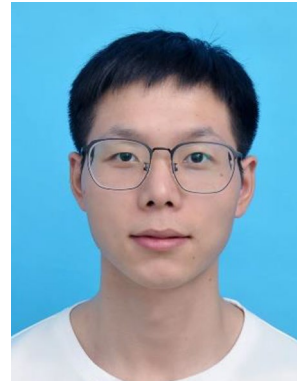


Fan Yang Fan Yang is a Professor in School of Energy and Environment at Southeast University. He received his Ph.D. from the Harbin Institute of Technology. His main research areas are solar energy technology, solid oxide fuel cells and semiconductor-ionic fuel cells.



Muhammad Afzal Muhammad Afzal is a Scientist in Energy Technology and Project Manager at KTH Royal Institute of Technology Sweden since May 2013. He is an experienced and enthusiastic researcher and teacher specialising in the investigation of new materials and electrochemical processes for energy conversion technologies. His work in the field of solid oxide fuel cell (SOFC) and electrolyte-layer free fuel cell (EFFC) has been acknowledged worldwide

as an emerging scientist and speaker. Dr Afzal obtained his Ph.D from KTH Royal Institute of Technology, Sweden in 2019. He is a committed and result oriented researcher equally in conventional fuel cells and EFFCs based on advanced and semiconductor-ionic materials. He is looking forward to new strategies in energy technologies and related materials.



Wanli Sun Wanli Sun is a master candidate in School of Energy and Environment at Southeast University, graduated from Zhengzhou University with a bachelor's degree, his current research direction is semiconductor ionic fuel cells.



Jung-Sik Kim Jung-Sik Kim is a Professor in Energy Technology & Demand Reduction in the École centrale de Pékin and in the School of General Engineering at Beihang University, China, since June 2021. He obtained his Ph.D at the University of Birmingham, UK in 2006. He is an experienced researcher and teacher specialising in the investigation of thermo-electrochemical processes for energy conversion and energy storage technologies whilst the majority part of his career has been developed at various institutes in the UK. He is proud of recent advances in semiconductor-ionic fuel cells whilst appreciating the international collaboration.